Journal of the European Ceramic Society 45 (2025) 117132

Contents lists available at ScienceDirect

Journal of the European Ceramic Society

journal homepage: www.elsevier.com/locate/jeurceramsoc

Pressureless synthesis and consolidation of the entropy-stabilized $(Hf_{0.25}Zr_{0.25}Ti_{0.25}V_{0.25})B_2$-$B_4C$ composite by ultra-fast high-temperature sintering (UHS)

Ana C. Feltrin [a], Emanuele De Bona [b], Levent Karacasulu [b,c], Mattia Biesuz [b], Vincenzo M. Sglavo [b,d], Farid Akhtar [a,*]

[a] *Division of Materials Science, Luleå University of Technology, Luleå 97187, Sweden*
[b] *Department of Industrial Engineering, University of Trento, Via Sommarive 9, Trento 38123, Italy*
[c] *Department of Materials Science and Engineering, Izmir Institute of Technology, İzmir 35430, Turkey*
[d] *INSTM, Trento Research Unit, Via G.Giusti 9, Firenze 50121, Italy*

ARTICLE INFO

Keywords:
Entropy-stabilization
Ultra-high-temperature ceramics
Ultra-fast high-temperature sintering

ABSTRACT

Entropy-stabilized Ultra High-Temperature Ceramics (UHTC) offer a groundbreaking solution to the challenges of extreme environments, showcasing enhanced mechanical properties, thermal stability, and resistance to oxidation at high temperatures. The consolidation of UHTC by ultra-fast high-temperature sintering (UHS) significantly reduces processing times and temperature and can produce dense high-performance ceramics with superior mechanical properties. This study reports the pressureless synthesis and consolidation of the entropy-stabilized $(Hf_{0.25}Zr_{0.25}Ti_{0.25}V_{0.25})B_2$-$B_4C$ composite through UHS within 1 minute, starting from transition metal diboride powders. B_4C acts as an effective sintering aid, promoting the densification of the system and the formation of a nearly single-phase hexagonal diboride with a diboride-eutectic phase. Furthermore, a secondary minor hexagonal phase rich in V and Zr is formed close to the eutectic regions. Sintering currents of 40 A were necessary to reach densities higher than 90 % under pressureless conditions, achieving nano hardness higher than 27.3 GPa, comparable with high-entropy diborides produced by Spark Plasma Sintering. The study highlights the entropy-stabilized phase formation, diffusion, densification, and grain growth mechanisms involved during UHS. The work contributes to the understanding of entropy-stabilized ceramics produced by UHS as a faster and less energy-consuming process than conventional sintering methods.

1. Introduction

Transition metal diborides (TMB_2s) uniquely combine metallic, ionic, and covalent bonding [1]. TMB_2s present an exceptional combination of ceramic-like characteristics, featuring high hardness ($>$ 20 GPa) and Young's modulus of approximately 500 GPa, alongside metal-like attributes such as high thermal and electrical conductivities (60–120 $W\,m^{-1}\,K^{-1}$ and $\sim 10^7$ $S\,m^{-1}$, respectively) [2].

Recent research within the Ultra High Temperature Ceramics (UHTC) has highlighted the need for a more systematic approach to understanding the contributions of each component in its composition. These investigations have considered the crucial influence of entropy in multicomponent systems and their thermo-mechanical properties [3]. Entropy is expected to dominate in stabilizing single-phase multicomponent ceramics [4], offering new pathways for synthesis and enabling property optimization without relying on toxic, scarce, or costly elements [5]. In this context, disorder plays an important role in enhancing the synthesizability and modifying the properties of entropy-stabilized ceramics [6], which are materials typically composed of disordered transition metal cation sublattices where, by increasing the configurational entropy in the system, it is possible to obtain new phases thermodynamically by lowering the Gibbs energy ($\Delta G_{mix} = \Delta H_{mix} - T\Delta S_{mix}$), commonly resulting in a single-phase material [3,7,8].

UHTC usually require high temperatures and external pressure to sinter due to their strong covalent bonds and limited grain boundary diffusion [9]. To further enhance UHTC densification, the introduction of suitable sintering aids becomes necessary, like deoxidizing aids, liquid phase additives, solid solution aids, etc. [10–12]. Metals such as

---

* Corresponding author.
E-mail address: farid.akhtar@ltu.se (F. Akhtar).

https://doi.org/10.1016/j.jeurceramsoc.2024.117132
Received 19 September 2024; Received in revised form 16 November 2024; Accepted 2 December 2024

Fe and Ni generate a liquid phase upon UHTC sintering, thus promoting rearrangement and mass transfer through the liquid medium by dissolution-precipitation mechanisms [9]. Diboride powder surface impurities, in particular oxides, can be effectively consumed by carbon and boron compounds like B, B_4C, C, WC, and phenolic resin, thus improving the sintering behavior of the system [13–21]. Adding B_4C and C to diborides promotes densification by reacting with the surface oxides and inhibits grain growth in pressureless sintering, for example, at 1900 °C for 2 h [22]. Besides the B_4C effect on the reduction of the surface oxide layer, its melting temperature is ~2400 °C, much lower than that of ZrB_2 and HfB_2 (>3250 °C).

Spark Plasma Sintering (SPS) is the predominant sintering technique for achieving dense entropy-stabilized UHTC. The first high-entropy diboride (HEB) was successfully produced using SPS at 2000 °C for 5 min, using transition metal diboride powders subjected to high-energy ball milling as starting materials [23]. Gild et al. [24] introduced a new approach named reactive flash Spark Plasma Sintering (reaFSPS), which combines rapid SPS and the flash sintering technique to quickly densify high-entropy UHTC. The utilization of reaFSPS enabled the achievement of dense $(Ti_{0.2}Zr_{0.2}Hf_{0.2}Nb_{0.2}Ta_{0.2})B_2$ and $(Ti_{0.2}Zr_{0.2}Hf_{0.2}Nb_{0.2}Ta_{0.2})C$ ceramics, which contained 3 wt% graphite sintered in 120 s. While advanced sintering techniques can successfully yield dense high-entropy UHTC, conventional methods often involve sintering temperatures exceeding 1800°C, leading to increased energy consumption and the development of a coarse microstructure [9].

Ultra-fast high-temperature sintering (UHS) was developed in 2020 by Wang et al. [25], where the sintering of a green body was achieved within seconds by placing a pellet between two Joule-heated carbon felts, with an ultra-high heating rate of 10^3-10^4 °C/min achieved without the aid of external pressure. UHS has clear advantages over SPS, including a reduced processing time, "light heating elements" with low thermal capacity, simple experimental equipment, and the possibility of obtaining components with complex geometries [25–27]. Due to the use of thermally insulating graphite heating elements, the temperature within the felt can exceed 2500 °C, thus enabling the densification of different refractory compounds including SiC [28], Si_3N_4 [29], ZrB_2-based materials [30,31], WC [32], ZrC [33] and high-entropy carbides [34].

Xie et al. [35] sintered the first HEB using this methodology. In their work, the high-entropy composite powder was first produced by mixing the transition metal powders Mo, Zr, Ta, Ti, and W with elemental boron and black carbon and heating the mixture to 2000 K. The powder was pressed into pellets, and a rapid liquid-phase high-temperature sintering process was conducted at 3000 K for 2 min. The final product was a mix of a high-entropy diboride phase, boron carbide, and zirconium dodecaboride. One can observe that their approach includes two separate steps: the formation of HEB and its sintering by UHS.

Guo et al. [34] attributed the ultra-fast densification observed in HEB and HEB-HEC to different factors. Firstly, the high sintering temperature exceeding 2360 °C was highlighted for its role in enhancing atomic diffusion and mass transport, thereby facilitating densification [34]. Additionally, the high heating rate, around 1000 °C/min, allows it to pass through the low-temperature region rapidly, thus effectively reducing particle coarsening and maintaining a high driving force for densification [36]. Furthermore, low-melting point phases (CrB_2) can be emphasized as promoters of particle rearrangement and enhanced densification [34,37].

Different from previous approaches, the present work investigates the simultaneous synthesis and densification of HEB by UHS, starting with mono-element diboride powders. Based on previous work [38,39], the entropy-stabilized $(Hf_{0.25}Zr_{0.25}Ti_{0.25}V_{0.25})B_2$ system is studied. Since B_4C is a common sintering aid for transition metal diborides and previous experimental evidence pointed out its positive effect on the UHS of ZrB_2 [31], the composite $(Hf_{0.25}Zr_{0.25}Ti_{0.25}V_{0.25})B_2$ – 10 vol% B_4C was considered.

2. Materials and characterization

$(Ti_{0.25}V_{0.25}Zr_{0.25}Hf_{0.25})B_2$ was processed using transition metal diborides as precursors in equiatomic ratio of 0.25 HfB_2 + 0.25 ZrB_2 + 0.25 VB_2 + 0.25 TiB_2. The powders used for the synthesis were HfB_2 (99.5 %, 1–10 μm) and VB_2 (99.5 %, <10 μm) from Shanghai Xinglu Chemical Co. (China), TiB_2 (98 %, 3 μm) and ZrB_2 (99 %, 5 μm) from US Research Nanomaterials, Inc. (USA). The as-received powders were mixed in equiatomic ratio in a polypropylene jar and dry milled using WC balls as mixing medium for 30 min in air atmosphere. The mass ratio of ball-to-powder was 3:1.

The diboride powder was mixed with 10 vol% B_4C (TETRABOR® 3000 F by ESK Ceramics GmbH, particle size around 0.8 μm) for 30 min in an ultrasonic bath with the addition of methyl ethyl ketone as solvent. The proportion of composite powder to solvent was 1 g to 1 mL. The mixed powders were dried overnight at 150 °C and pressed uniaxially under 500 MPa into disc-shaped samples with a diameter of 6 mm. To carry out UHS experiments, a carbon felt (SGL Carbon Co., Germany) was clamped between two steel electrodes, thus creating an electrode span of 23 mm with a cross-section of 15×6 mm^2. The green specimens were inserted into the carbon felt through a small hole manually produced with a spatula. UHS was carried out in a borosilicate glass flask filled with argon gas. An electric current was applied to the carbon felt using a DC power supply (GW Instek, DC power supply PSU 30–50, Taiwan) for 1 min at different currents ranging from 30 A to 42.5 A.

For microstructure characterization, the specimens were ground and polished following standard sample preparation, and the mineralogical composition was characterized by X-ray diffraction (PANalytical Empyrean X-ray diffractometer, Malvern, UK) with 40 mA and 45 kV and Cu Kα radiation, scanning electron microscope (SEM, JSM-IT300, JEOL, Japan). The elemental distribution was analyzed using Energy-dispersive X-ray Spectroscopy (EDS), and the phase distribution was studied using Electron backscatter diffraction (EBSD). EBSD analysis was carried out using an acceleration voltage of 20 kV and a step size of 1.5 μm. AZtecCrystal (Oxford Instruments) software was used to post-process the obtained data (noise reduction).

Image Analysis software (MIPAR, USA) was used to determine grain size in the entropy-stabilized phase of the sintered specimens. Ten backscattered electron (BSE) images from each sintering current were considered.

The activation energy (E_a) for the grain growth of the high-entropy diboride (HEB) phase was determined using the Arrhenius equation, Eq. 1:

$$d = Ce^{\left(\frac{-E_a}{R\,T}\right)} \quad (1)$$

where d represents the estimated grain area (μm^2), T is the temperature, C is a constant, and R is the perfect gas constant (8.314 J/(mol K). The procedure used to estimate the temperature is reported in the Results & Discussion section.

To determine the mechanical properties, nanoindentation was performed at 200 mN load and 10 s dwell time on a polished surface with a Nano Test Vantage (Micro Materials, UK) equipped with a diamond Berkovich indenter. A matrix of 5 × 5 indents was considered to determine nano hardness, and Young's modulus was calculated using the unloading slopes (assuming Poisson's ratio equal to 0.149 [39]). After testing, the indents were analyzed by optical microscopy to filter out the indents close to pores and to identify the phase each indent was performed on. Microhardness was measured by applying 9.8 N and 4.5 N loads with 15 s dwell time using a Matsuzawa Hardness Tester (Matsuzawa Co., Ltd, Japan) equipped with Buehler Omnimet MHT Hardness Measurement system (Buehler Ltd., USA) and a diamond Vickers indenter.

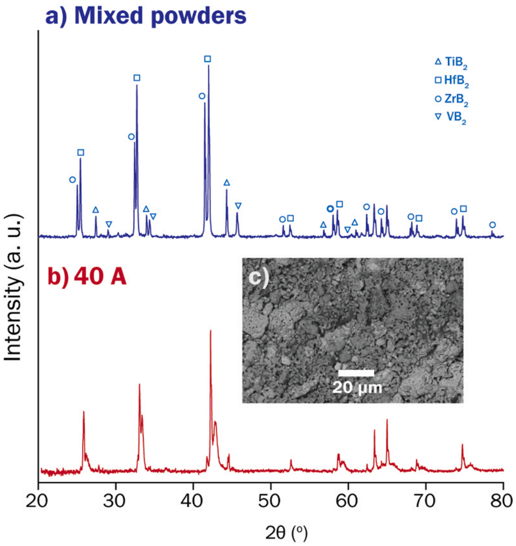

Fig. 1. X-ray diffractograms of the (a) diboride mixed powders and (b) diboride mixed powders sintered under 40 A for 60 s without sintering aid. SEM of the microstructure is shown in c.

3. Results and discussion

UHS of diboride powder without B_4C addition resulted in heterogeneous and porous microstructure even under high currents (i.e., 40 A) and did not stabilize a single phase. This can be evidenced by multiple diffraction peaks in the X-ray diffractograms showing a pattern similar to the mixed powder (Fig. 1a and b) and by the non-densified microstructure shown in Fig. 1c. The results indicate that adding a sintering aid is pivotal in obtaining dense components; therefore, B_4C was added to the mixture of diboride powders as sintering additive for further investigations.

The UHS temperature cannot be easily quantified as the sample position in the felt is not accessible with an IR pyrometer and using a shielded thermocouple can perturbate the system [40]. Nevertheless, a calibration procedure based on the melting points of pure compounds like Cu (1084 °C), Pt (1768 °C), Al_2O_3 (2051 °C), and B_4C (2350 °C) was performed to estimate the temperature reached within the felt for a specific applied current and power. The obtained function to determine the temperature reached during the sintering process is shown in Fig. 2. Moreover, based on previous FEM simulations, one can state that the temperature should approach the melting point of B_4C under 35 A [31], in agreement with the finding obtained during the present activity.

The power *versus* current relationship is not perfectly quadratic because the felt becomes more conductive at higher temperatures. The exponent of the power law correlating temperature and power is 0.34. In the case of pure radiation, it should be 0.25, but here, there is also a linear conduction term within the feltcontributing, making this result reasonable. At currents below 40 A, the felt should be hotter than the melting point of VB_2 (although the sintered material itself can be cooler than the felt, making an accurate temperature estimation challenging). During the sintering process, we estimate that the temperature reached approximately 2700 °C, which is higher than the melting point of VB_2.

The relative density of the $(Hf_{0.25}Zr_{0.25}Ti_{0.25}V_{0.25})B_2$-$B_4C$ increases from 70 % to 98 % when the UHS current rises from 30 to 42.5 A in 60 s treatments (Fig. 3). One can observe that the density monotonically increases with the applied current due to higher UHS temperature promoting mass transport and diffusion. Therefore, adding B_4C as sintering additive efficiently promoted densification, similar to what was previously reported for ZrB_2-B_4C composites [31].

At 40 A and 42.5 A, well-densified microstructure is obtained. It is worth pointing out that the entire process was completed in 1 min, i.e., with a processing time about 50 times shorter than what is typically required to obtain these compounds by SPS (including the cooling step from high temperature). The density of the specimens produced using 42.5 A is higher than 40 A; in addition, the specimens obtained under 40 A still maintain the sharp features of their geometrical shape, whereas under 42.5 A the pellet corners start to get rounded (Fig. 3) as a

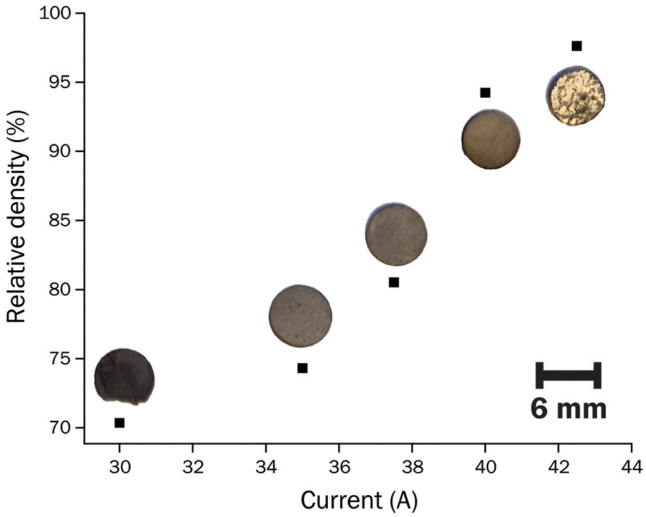

Fig. 3. Density as a function of the current used for ultra-fast high-temperature sintering for 60 s.

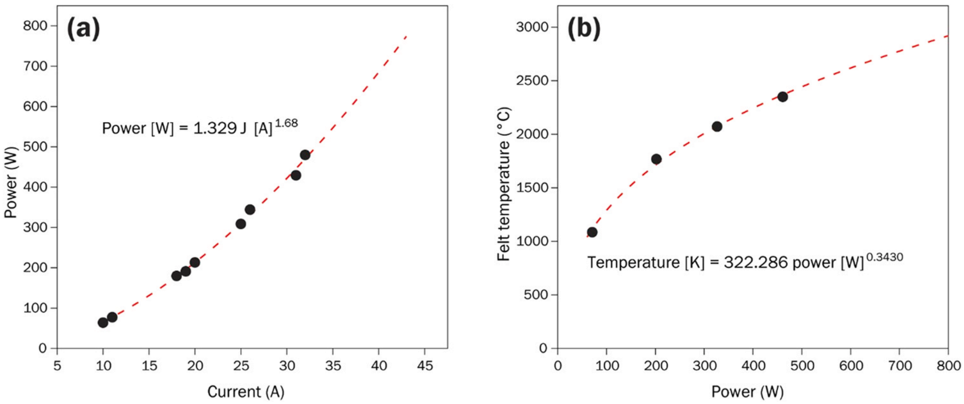

Fig. 2. Calibration of the felt temperature. (a) Relation between applied power and current and (b) relation between temperature and power (the experimental points are black while the dashed lines represent the fitting curves).

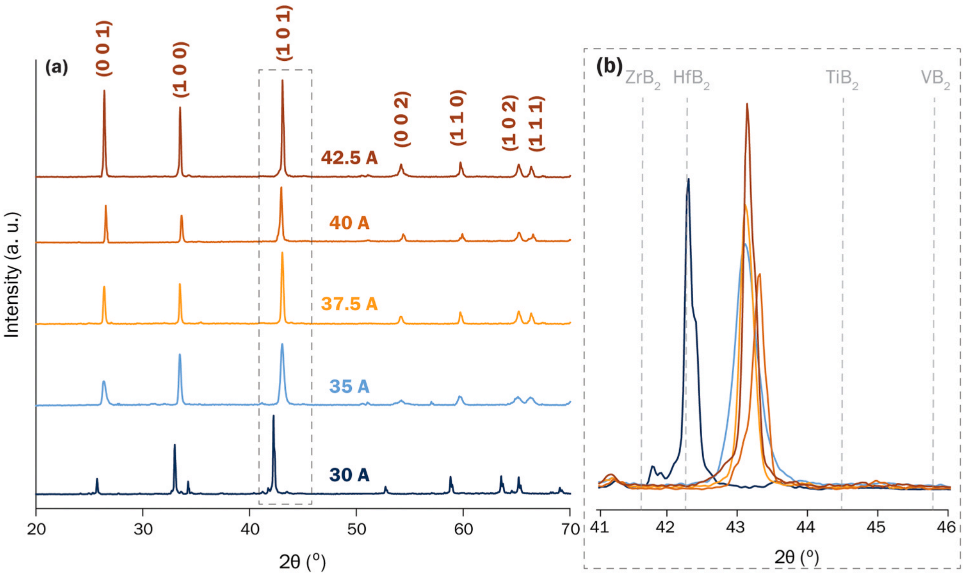

Fig. 4. X-ray diffractograms of the diborides as a function of the UHS current for the 2θ range (a) 20–70° and (b) zoom in the $2\theta = 41$–46° region.

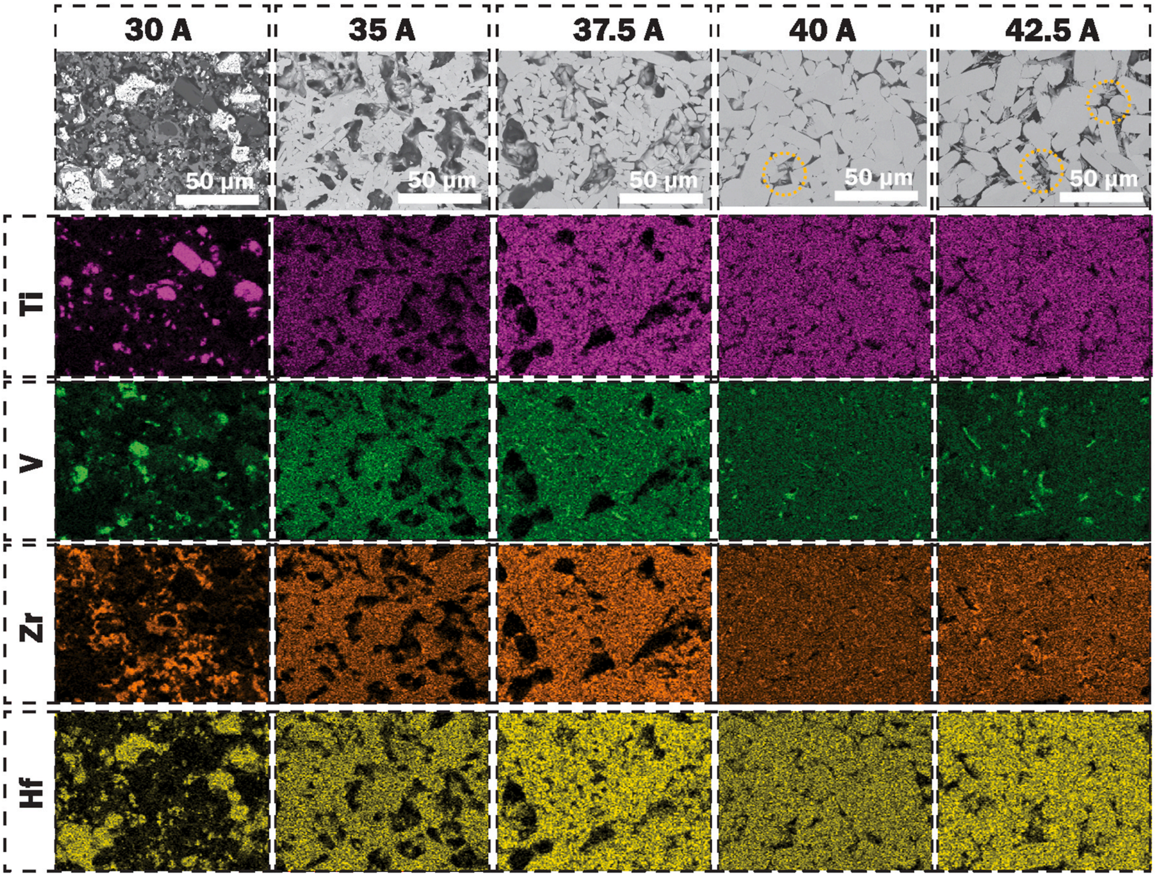

Fig. 5. SEM micrographs and EDS maps of the diborides sintered using 30–42.5 A. Yellow circles mark areas with eutectic formation on SEM in the diborides sintered at 40 and 42.5 A.

result of the formation of a larger volume of liquid. As such, the processing window to densify this composite with shape retention is extremely narrow, and particular care must also be taken in positioning the pellet in the center of the felt.

Fig. 4a shows the X-ray diffractogram of the sintered specimens. All specimens show single- or dual-phase composition, retaining the hexagonal structure of the initial diboride powders. Fig. 4b presents a magnified view of the (1 0 1) peak, with a comparison of the 2θ peak position for the precursor diborides.

We previously observed that the pure system, not including B_4C, is multi-phase even under 40 A (Fig. 1b). Indeed, the limited mass transport phenomena from the diborides hindered sintering and the solid-

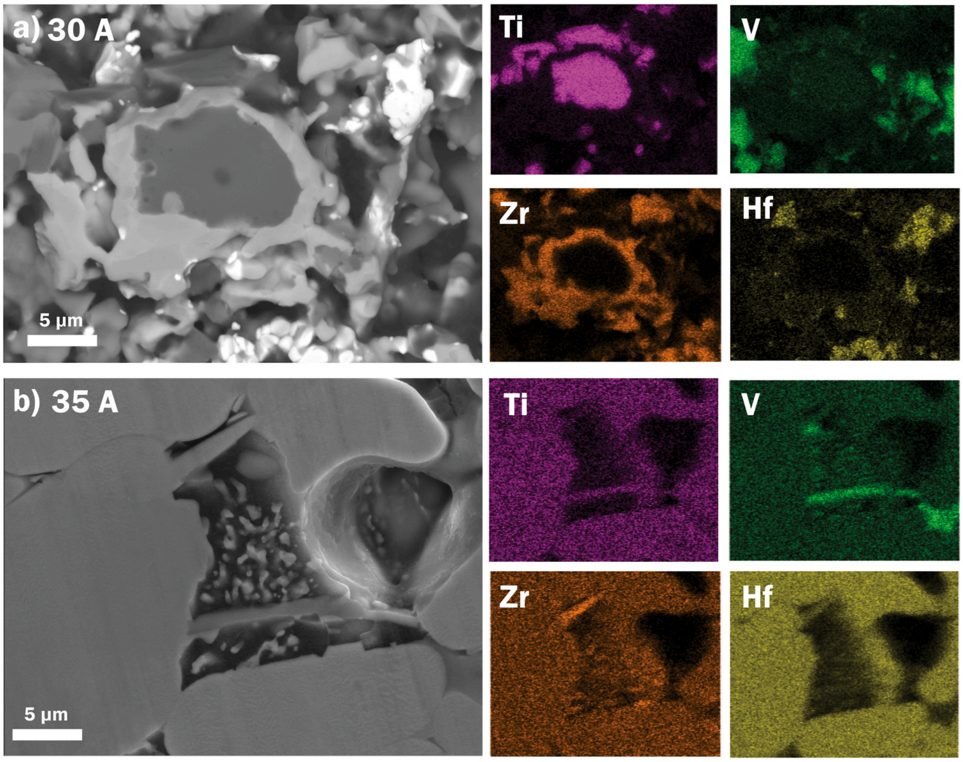

Fig. 6. Higher magnification SEM-EDS images of the composites produced at (a) 30 A and (b) 35 A.

state reaction. The results are much more encouraging when considering the composite including a B_4C as sintering additive. A peak separation is evident at a current of 30 A, and a discernible "shoulder" appears on the (1 0 1) peak. This is likely due to hexagonal phases with different lattice parameters, with the peaks for HfB_2 and ZrB_2 appearing much stronger than those for TiB_2 and VB_2, as observed for the mixed powders in Fig. 1a.

By increasing the sintering current, the (1 0 1) peak (Fig. 4b) consistently shifts to the higher angle, resulting in a d-spacing between what is expected for ZrB_2 - HfB_2 and TiB_2 - VB_2. This suggests a more homogeneous cation distribution with increasing UHS current and temperature. Furthermore, the diffraction peaks (Fig. 4a) are observed to become narrower and more intense as the current increases. Notably, B_4C peaks are not detectable by XRD analysis. This is attributed to its small atomic number and low electron density, overshadowed by the much stronger peaks of HEB [35]. More about the presence of B_4C in the sintered materials is discussed in the following sections.

While a perfectly ideal solid solution was not fully obtained, as indicated by the presence of minor peaks and shoulders in the XRD (Fig. 4), one can observe that UHS is very effective in the simultaneous synthesis and sintering of HEB components. Moreover, one can infer that adding B_4C led to an efficient sintering and stabilization of HEB. It is interesting to notice that a nearly single-phase HEB formation occurs using a current of 35 A in 60 s, i.e., well before densification occurs.

Fig. 5 shows the microstructure and distribution of cations after sintering. At 30 A, the diboride particles initiate sintering with a light necking effect. The EDS maps show an inhomogeneous cations distribution corroborating the presence of multiple phases as detected by XRD. At 30 A, the grains are still largely equiaxial and minor evidence of liquid phase formation upon UHS is found. Sintering at 35 A causes a clear evolution of the material but results in relatively large pores/voids. The porous microstructure agrees with the density results (Fig. 3), indicating a relative density of ≈ 70 %. Besides the modest densification, sintering at 35 A shows an apparent change in the grain size and shape compared to 30 A. Grain coarsening occurred leading to the formation of large HEB elongated grains within a molten B_4C-rich matrix

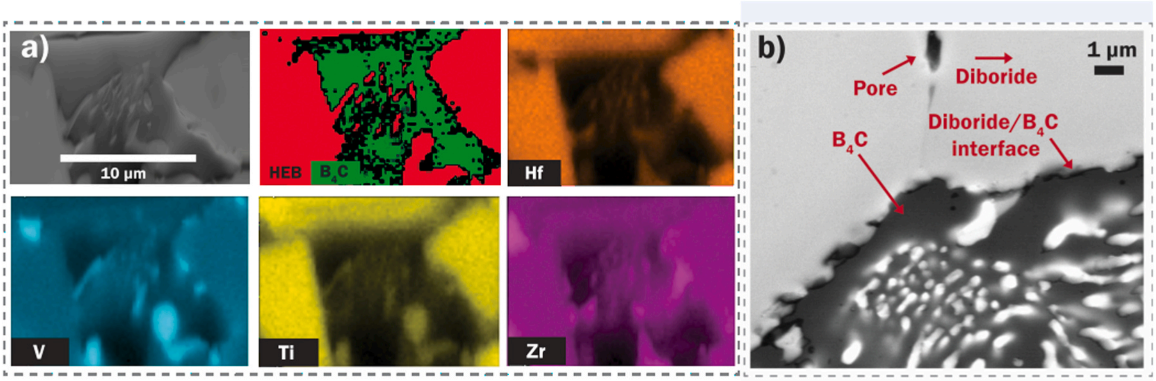

Fig. 7. (a) EDS and EBSD of the B_4C phase between HEB grains and (b) SEM image using 3 kV in the specimen produced by UHS under 42.5 A.

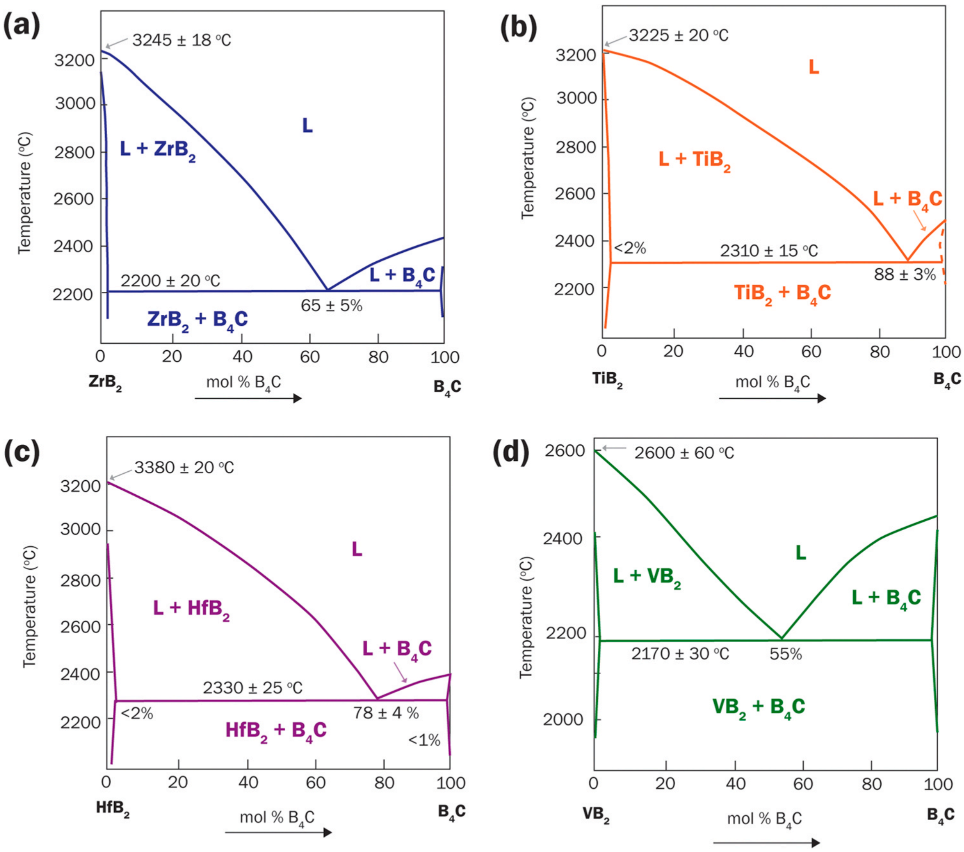

Fig. 8. Phase diagrams of TMB$_2$-B$_4$C compositions. ZrB$_2$ (a), TiB$_2$ (b) and HfB$_2$ (c) from [49] and VB$_2$ (d) from [50].

based on the anisotropy of the diborides crystal structure [41]. Usually, substantial grain size and shape alteration are features encountered in the final sintering stage; herein, we observe these in the early intermediate stage. The EDS map shows a homogeneous distribution of the cations that is in agreement with the formation of the HEB solid solution. The microstructure also shows evidence of liquid phase formation in accord with the calibrated felt temperature exceeding the melting point of B$_4$C (> 35 A).

Sintering at 40 A and 42.5 A yields similar structures, which are generally denser and coarser at increasing the applied current, corroborating the density measurements. The overall cation distribution shows a well-dispersed distribution of Ti, Hf, and Zr, but V (and marginally Zr) partially segregates close to the grain boundaries. One can note that B$_4$C mainly constitutes the dark inter-grain regions in the micrographs and are not pores (Fig. 6). The final microstructure (42.5 A, $T \approx 2800^{\circ}C$) includes the typical features of liquid phase sintering, with large and rounded grains and a secondary phase infiltrating the grain boundary.

Fig. 6 presents a higher magnification SEM-EDS of the 30 A and 35 A sintered microstructures to understand the cation's behavior better. Fig. 6a, shows evidence of diffusion among some cations, with Zr and Ti particles beginning to diffuse, while Hf has initiated "necking" to Zr-concentrated areas. The onset of diffusion can be primarily attributed to the similar formation enthalpy of Ti, Zr, and Hf diborides ($TiB_2 = -83$, $HfB_2 = -95$, $ZrB_2 = -104$, in kJ/mol [42]), where closer formation enthalpy promotes affinity for dissolution between the phases. Conversely, VB$_2$, with a formation enthalpy of -53 kJ/mol [42], requires more energy for diffusion and appears more segregated. Under 35 A, even though a homogeneous a single-phase can be identified, some heterogeneity can be observed in columnar grains closer to the eutectic regions (Fig. 6b).

As previously discussed, the darker contrast phase is expected to be B$_4$C near the grain boundaries. In Fig. 7, a high-resolution SEM image of the structure from the 42.5 A specimen aims to discern whether B$_4$C is still present after sintering as a secondary phase. Given the limitations in EDS reliability for B and C, EBSD was performed to identify the B$_4$C phase. For the HEB phase, XRD-derived d-space, was used. The dark phase surrounding the HEB particles and grain boundaries matches the diffraction features related to B$_4$C. Moreover, one can observe the formation of a eutectic microstructure, as evidenced by adjacent lamellar structures (Fig. 6b and Fig. 7a and b). Notably, the cation distribution reveals a pronounced V-Ti and a minor Zr-Hf segregation around the B$_4$C particles. Despite this localized heterogeneity in the distribution of cations within the hexagonal HEB phase, EBSD analysis detects only one hexagonal phase, indicating that the different cation distribution does not substantially impact on the d-spacing of the solid solution.

It is important to emphasize that a high-entropy phase was technically achieved for sintering currents exceeding 35 A, as evidenced by the cation's distribution falling within the range of 5–35 at%. This strongly suggests that the high-entropy phase formation precedes the material densification, and this indicates that diffusion occurs faster than in other sintering methods, similar to that described as the primary densification mechanism for ZrB$_2$ at temperatures higher than 2000 °C [43].

The affinity of the sintering aid with the metallic diborides influences the arrangement of the cation's distribution surrounding B$_4$C. Fig. 8 shows the phase diagrams of the TMB$_2$ and B$_4$C. All the phase diagrams present a eutectic point with liquid phase formation by reaction between B$_4$C and TMB$_2$. In the VB$_2$-B$_4$C system, the eutectic temperature is ~2170°C, followed by the ZrB$_2$-B$_4$C system at ~2200°C, and subsequently by TiB$_2$- and HfB$_2$-B$_4$C systems at temperatures exceeding 2310 °C. Moreover, one can observe that the eutectic liquid composition is higher in the concentration of VB$_2$ (45 %) and ZrB$_2$ (35 %) compared with HfB$_2$ (22 %) and TiB$_2$ (12 %). Finally, the solubility of V and Zr at the sintering temperature in the liquid is much larger than that of Hf and Ti as the liquidus line in the first two cases is shifted to the left side of the

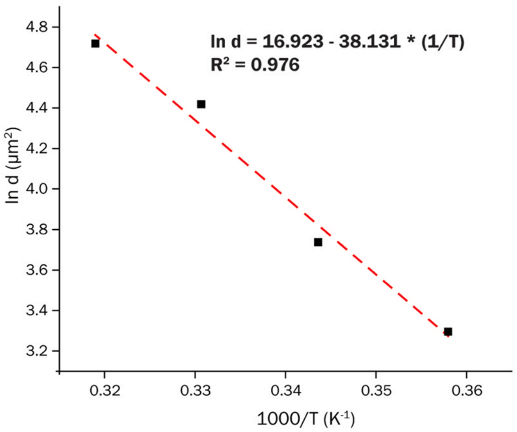

Fig. 9. Arrhenius plot of the estimated grain area *versus* sintering temperature.

diagrams in Fig. 8. Hence, when the solidification starts, the liquid phase is V- and Zr-rich, which is held until the solidification is completed (i.e., at the eutectic temperature) thus crystallizing a Zr- and V-rich diboride in columnar grains close to the melted region. These diborides formed during the rapid solidification process preferentially grow on the edge of the molten region on the surface of the primary (not molten while sintering) diborides grains, producing the so-called “divorced eutectic” microstructure. These features are visible in Fig. 6 and Fig. 7. Notably, VB_2 exhibits the lowest melting point among the diborides, suggesting the potential occurrence of partial melting around the sintering aid particles during the sintering process.

Most of the studies to date have discussed densification of HEB that are nominally single phase, at least by XRD. However, other researchers have noted phase segregation in the final HEB [44–48]. The analysis of $(HfNbTaTiZr)B_2$ by XRD was consistent with a ceramic that was nominally a single-phase, but analysis by SEM and EDS revealed the presence of an Nb-rich second phase that appeared as dark regions in SEM [44]. The hypothesis was that the Nb-rich regions had the same crystal structure as the main diboride phase with nearly identical lattice parameters.

The analysis of the estimated grain area was carried out for 35, 37.5, 40, and 42.5 A specimens, and micro- and nano hardness for the 40 and 42.5 A (>90 % relative density) specimens. Notably, the grain growth of the HEB becomes increasingly evident at higher sintering current, which mostly contributes to the observed peak broadening, which primarily correlates with smaller crystallites [51], described as shown in Fig. 4. As the current increases from 30 to 42.5 A, the area of the HEB grains rises from ~27 μm^2 to ~112 μm^2. A higher current is essential to achieve a corresponding increase in density, but as previously discussed, it did not change the composition of the entropy-stabilized phase that was formed during sintering. Concerning the densification process, the activation energy is a significant physical parameter that characterize the material transport mechanism during grain growth.

The activation energy relationship based on Eq. 1, is shown in Fig. 9. The linear regression results allow us to estimate an activation energy of 317 kJ/mol for HEB phase grain growth. Lonergan et al. [43] reported that lattice diffusion was the primary sintering mechanism for ZrB_2, at temperatures up to 2000 °C, with $E_a = 241 \pm 62$ kJ/mol. In comparison, the sintering activation energy for (TiZrHfVNbTa)C was 839 ± 53 kJ/mol [52], also associated with lattice diffusion, while for TiC with 390 kJ/mol [52] grain boundary diffusion was the primary mechanism. In the present HEB phase, the densification process involves a solid-state grain boundary diffusion and material transport through a transient liquid phase, which takes place at the grain boundaries, improving the ceramic densification.

Previously, load-dependent hardness has been shown in high-entropy ceramics, where the hardness decreases with increasing load [46,53,54], but this trend is not evident for the present composite, very likely because of its porosity. Since the nanoindentation loads do not exceed the depth of 1 µm, the likelihood of encountering any pores during the measurement was minimized. Here, the hardness of the sintered specimens is not significantly higher than that calculated by the rule of mixture for the diborides, 24.7 GPa [55–57], for both 40 A (22.4 ± 1.8 and 27.3 ± 1.2 GPa for 4.9 N and 1.96 N, respectively) and 42.5 A sintered composites (24.1 ± 1.9 and 28.7 ± 0.9 GPa for 4.9 N and 1.96 N, respectively). The values are comparable with the single-phase high entropy diboride $(Ti_{0.2}Zr_{0.2}Nb_{0.2}Hf_{0.2}Ta_{0.2})B_2$, with a density of 99 % and micro hardness of 20.2 GPa [53], density of 96.3 % and hardness of 21.7 ± 0.7 GPa [47] and density of 97.7 % and hardness of 26.3 ± 0.7 GPa [46], and it is lower than the single-phase diboride with the same composition manufactured by SPS (33.2 ± 2.1 GPa micro-hardness at 9.8 N, 29.8 ± 3.4 GPa nano hardness at 1.96 mN) and Young’s modulus of 466.0 ± 5.9 GPa [39].

Some of the microhardness imprints at 9.8 N on specimens processed under 40 A are shown in Fig. 10. The material does not resist such load, probably due to its high porosity. However, it is possible to see that the fracture mechanism of the grains is predominantly intragranular, and crack-deflecting mechanisms are not operating [22]. Moreover, it seems that the grain boundaries are weaker than in SPS samples [39] and the grains can “slip out” of the microstructure instead of cracking which is probably related to the lower hardness of the UHS material. Moreover, the not-fully dense structure and the residual thermal stresses resulting from the differences in the thermal expansion coefficient of the HEB and B_4C might have also weakened the material.

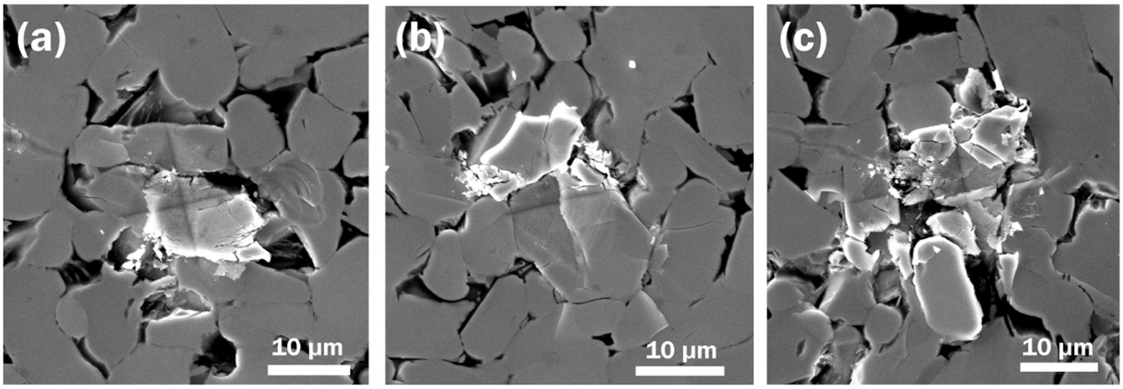

Fig. 10. Imprints produced during micro indentation on the surface of the specimen processed under 40 A by 9.8 N loads. (a) and (b) intragranular fracture phenomena, without crack deflection by the sintering aid; (c) shattering fracture with grain “pull out”.

4. Conclusions

This study demonstrates the significant potential of ultra-fast high-temperature sintering (UHS) to consolidate entropy-stabilized Ultra-high Temperature Ceramics, namely, $(Hf_{0.25}Zr_{0.25}Ti_{0.25}V_{0.25})B_2$-$B_4C$ composite. Utilizing UHS, we achieved the simultaneous synthesis and densification of entropy-stabilized diboride from transition metal element diboride powders and B_4C, significantly reducing processing time and avoiding the need for pressure application. Remarkably, the reaction between the mono-element diborides was completed within one minute through by forming a eutectic liquid originating from the reaction between B_4C and MB_2. The hardness of the composite is fully comparable with that of the same composition obtained by Spark Plasma Sintering. All the process was completed in 1 min about 50 times faster than what typically required to obtain these compounds by SPS. The study contributes to understanding the sintering behavior and mechanical properties of HEB-B_4C composites sintered using UHS, and a wide range of compositions are still to be investigated using this versatile sintering method.

CRediT authorship contribution statement

Emanuele De Bona: Methodology, Investigation. **Ana C. Feltrin:** Writing – original draft, Validation, Methodology, Investigation, Formal analysis, Data curation, Conceptualization. **Levent Karacasulu:** Methodology, Investigation. **Vincenzo M. Sglavo:** Writing – review & editing, Supervision, Resources, Funding acquisition. **Mattia Biesuz:** Writing – review & editing, Writing – original draft, Validation, Supervision, Methodology. **Farid Akhtar:** Writing – review & editing, Writing – original draft, Validation, Supervision, Resources, Project administration, Investigation, Funding acquisition, Conceptualization.

Declaration of Competing Interest

The authors declare that they have no known competing financial interests or personal relationships that could have appeared to influence the work reported in this paper.

Acknowledgements

This work was supported by the Swedish Foundation for Strategic Research (SSF) for Infrastructure Fellowship, Grant No. RIF14–0083. The authors acknowledge Erik Nilsson for the help with the EBSD and the LUMIA (Luleå Material Imaging and Analysis) center for providing the imaging characterization equipment.

References

[1] A. Fleurence, R. Friedlein, T. Ozaki, H. Kawai, Y. Wang, Y. Yamada-Takamura, Experimental evidence for epitaxial silicene on diboride thin films, Phys. Rev. Lett. (2012), https://doi.org/10.1103/PhysRevLett.108.245501.

[2] T. Endo, S. Nakane, M. Kato, K. Hirota, T. Nishimura, K. Mizuuchi, Y. Morisada, Engineering properties of borides, ceramics and glasses, Eng. Mater. Handb. (1991).

[3] A. Nisar, T. Dolmetsch, T. Paul, T.S. Sakthivel, C. Zhang, B. Boesl, S. Seal, A. Agarwal, Unveiling enhanced oxidation resistance and mechanical integrity of multicomponent ultra-high temperature carbides, J. Am. Ceram. Soc. (2022), https://doi.org/10.1111/jace.18281.

[4] C. Toher, C. Oses, D. Hicks, S. Curtarolo, Unavoidable disorder and entropy in multi-component systems, NPJ Comput. Mater. (2019), https://doi.org/10.1038/s41524-019-0206-z.

[5] C. Toher, C. Oses, M. Esters, D. Hicks, G.N. Kotsonis, C.M. Rost, D.W. Brenner, J. P. Maria, S. Curtarolo, High-entropy ceramics: propelling applications through disorder, MRS Bull. (2022), https://doi.org/10.1557/s43577-022-00281-x.

[6] C. Oses, C. Toher, S. Curtarolo, High-entropy ceramics, Nat. Rev. Mater. (2020), https://doi.org/10.1038/s41578-019-0170-8.

[7] M. Qin, Q. Yan, Y. Liu, H. Wang, C. Wang, T. Lei, K.S. Vecchio, H.L. Xin, T. J. Rupert, J. Luo, Bulk high-entropy hexaborides, J. Eur. Ceram. Soc. (2021), https://doi.org/10.1016/j.jeurceramsoc.2021.05.027.

[8] T. Wen, B. Ye, M.C. Nguyen, M. Ma, Y. Chu, Thermophysical and mechanical properties of novel high-entropy metal nitride-carbides, J. Am. Ceram. Soc. (2020), https://doi.org/10.1111/jace.17333.

[9] D. Ni, Y. Cheng, J. Zhang, J.X. Liu, J. Zou, B. Chen, H. Wu, H. Li, S. Dong, J. Han, X. Zhang, Q. Fu, G.J. Zhang, Advances in ultra-high temperature ceramics, composites, and coatings, J. Adv. Ceram. (2022), https://doi.org/10.1007/s40145-021-0550-6.

[10] Z. Tan, M. Zhang, S. Zhao, Y. Huang, Z. Huang, Microstructure, mechanical and friction-wear properties of SiC-WC composite with Al and C as sintering aids, J. Eur. Ceram. Soc. 44 (2024) 3557–3568, https://doi.org/10.1016/j.jeurceramsoc.2024.01.009.

[11] J.-X. Liu, G.-J. Zhang, F.-F. Xu, W.-W. Wu, H.-T. Liu, Y. Sakka, T. Nishimura, T. S. Suzuki, D.-W. Ni, J. Zou, Densification, microstructure evolution and mechanical properties of WC doped HfB2–SiC ceramics, J. Eur. Ceram. Soc. 35 (2015) 2707–2714, https://doi.org/10.1016/j.jeurceramsoc.2015.04.009.

[12] K. Raju, D.-H. Yoon, Sintering additives for SiC based on the reactivity: a review, Ceram. Int 42 (2016) 17947–17962, https://doi.org/10.1016/j.ceramint.2016.09.022.

[13] X.G. Wang, W.M. Guo, G.J. Zhang, Pressureless sintering mechanism and microstructure of ZrB2-SiC ceramics doped with boron, Scr. Mater. (2009), https://doi.org/10.1016/j.scriptamat.2009.03.030.

[14] D.W. Ni, J.X. Liu, G.J. Zhang, Pressureless sintering of HfB 2-SiC ceramics doped with WC, J. Eur. Ceram. Soc. (2012), https://doi.org/10.1016/j.jeurceramsoc.2012.05.001.

[15] J. Zou, S.K. Sun, G.J. Zhang, Y.M. Kan, P.L. Wang, T. Ohji, Chemical reactions, anisotropic grain growth and sintering mechanisms of self-reinforced ZrB2-SiC doped with WC, J. Am. Ceram. Soc. (2011), https://doi.org/10.1111/j.1551-2916.2010.04278.x.

[16] J. Zou, G.J. Zhang, Y.M. Kan, Formation of tough interlocking microstructure in ZrB2-SiC-based ultrahigh-temperature ceramics by pressureless sintering, J. Mater. Res. (2009), https://doi.org/10.1557/jmr.2009.0274.

[17] M. Shahedi Asl, M. Ghassemi Kakroudi, Characterization of hot-pressed graphene reinforced ZrB2-SiC composite, Mater. Sci. Eng.: A (2015), https://doi.org/10.1016/j.msea.2014.12.028.

[18] A.L. Chamberlain, W.G. Fahrenholtz, G.E. Hilmas, Low-temperature densification of zirconium diboride ceramics by reactive hot pressing, J. Am. Ceram. Soc. (2006), https://doi.org/10.1111/j.1551-2916.2006.01299.x.

[19] S.C. Zhang, G.E. Hilmas, W.G. Fahrenholtz, Pressureless densification of zirconium diboride with boron carbide additions, J. Am. Ceram. Soc. (2006), https://doi.org/10.1111/j.1551-2916.2006.00949.x.

[20] L. Rangaraj, C. Divakar, V. Jayaram, Fabrication and mechanisms of densification of ZrB2-based ultra high temperature ceramics by reactive hot pressing, J. Eur. Ceram. Soc. (2010), https://doi.org/10.1016/j.jeurceramsoc.2009.08.003.

[21] S. Ran, O. Van der Biest, J. Vleugels, ZrB2-SiC composites prepared by reactive pulsed electric current sintering, J. Eur. Ceram. Soc. (2010), https://doi.org/10.1016/j.jeurceramsoc.2010.05.012.

[22] S. Zhu, W.G. Fahrenholtz, G.E. Hilmas, S.C. Zhang, Pressureless sintering of zirconium diboride using boron carbide and carbon additions, J. Am. Ceram. Soc. (2007), https://doi.org/10.1111/j.1551-2916.2007.01936.x.

[23] J. Gild, Y. Zhang, T. Harrington, S. Jiang, T. Hu, M.C. Quinn, W.M. Mellor, N. Zhou, K. Vecchio, J. Luo, High-entropy metal diborides: a new class of high-entropy materials and a new type of ultrahigh temperature ceramics, Sci. Rep. 6 (2016) 2–11, https://doi.org/10.1038/srep37946.

[24] J. Gild, K. Kaufmann, K. Vecchio, J. Luo, Reactive flash spark plasma sintering of high-entropy ultrahigh temperature ceramics, Scr. Mater. (2019), https://doi.org/10.1016/j.scriptamat.2019.05.039.

[25] C. Wang, W. Ping, Q. Bai, H. Cui, R. Hensleigh, R. Wang, A.H. Brozena, Z. Xu, J. Dai, Y. Pei, C. Zheng, G. Pastel, J. Gao, X. Wang, H. Wang, J.C. Zhao, B. Yang, X. Zheng, J. Luo, Y. Mo, B. Dunn, L. Hu, A general method to synthesize and sinter bulk ceramics in seconds, Science 1979 (2020), https://doi.org/10.1126/science.aaz7681.

[26] S. Bhandari, C. Manière, F. Sedona, E. De Bona, V.M. Sglavo, P. Colombo, L. Fambri, M. Biesuz, G. Franchin, Ultra-rapid debinding and sintering of additively manufactured ceramics by ultrafast high-temperature sintering, J. Eur. Ceram. Soc. (2024), https://doi.org/10.1016/j.jeurceramsoc.2023.08.040.

[27] F. Zuo, Q. Wang, Z.Q. Yan, M. Kermani, S. Grasso, G.L. Nie, B.B. Jiang, F.P. He, H. T. Lin, L.G. Wang, Upscaling ultrafast high-temperature sintering (UHS) to consolidate large-sized and complex-shaped ceramics, Scr. Mater. (2022), https://doi.org/10.1016/j.scriptamat.2022.114973.

[28] F. Zuo, Y.N. Deng, Z.X. Liu, Q. Li, S. Grasso, Y.X. Xu, B.B. Jiang, Q.G. Jiang, H. T. Lin, L.G. Wang, Enhancing densification rate and the unusual 4H-SiC polytype stabilization in ultrafast high-temperature sintering of α-SiC, J. Eur. Ceram. Soc. 44 (2024) 610–616, https://doi.org/10.1016/j.jeurceramsoc.2023.09.038.

[29] R.X. Luo, M. Kermani, Z.L. Guo, J. Dong, C.F. Hu, F. Zuo, S. Grasso, B.B. Jiang, G. L. Nie, Z.Q. Yan, Q. Wang, Y.L. Gan, F.P. He, H.T. Lin, Ultrafast high-temperature sintering of silicon nitride: a comparison with the state-of-the-art techniques, J. Eur. Ceram. Soc. (2021), https://doi.org/10.1016/j.jeurceramsoc.2021.06.021.

[30] S. Mondal, J.D.S. Lombard, S. Gollapudi, C. Tallon, J.F. Li, D. Viehland, Ultrafast high-temperature sintering of ZrB2, J. Am. Ceram. Soc. (2024), https://doi.org/10.1111/jace.19445.

[31] E. De Bona, C. Manière, V.M. Sglavo, M. Biesuz, Ultrafast high-temperature sintering (UHS) of ZrB2-based materials, J. Eur. Ceram. Soc. (2024), https://doi.org/10.1016/j.jeurceramsoc.2023.09.007.

[32] E. De Bona, L. Karacasulu, C. Vakifahmetoglu, V.M. Sglavo, M. Biesuz, Ultrafast high-temperature sintering (UHS) of WC and WC-containing ZrB2, J. Alloy. Compd. 986 (2024) 174102, https://doi.org/10.1016/j.jallcom.2024.174102.

[33] B. Zhang, M. Hu, F. Zhong, S. Zhang, Z. Yang, X. Qiu, J. Xu, J. Ou-Yang, Y. Zhang, B. Zhu, X. Yang, S. Chen, Ultrafast high-temperature sintering and densification of ZrC-based ceramics, J. Eur. Ceram. Soc. 44 (2024) 5569–5578, https://doi.org/10.1016/j.jeurceramsoc.2024.03.037.

[34] R.-F. Guo, H.-R. Mao, P. Shen, Ultra-fast high-temperature synthesis and densification of high-entropy diborides and diboride-carbide ceramics, J. Eur. Ceram. Soc. 43 (2023) 5763–5773, https://doi.org/10.1016/j.jeurceramsoc.2023.05.042.

[35] H. Xie, M. Qin, M. Hong, J. Rao, M. Guo, J. Luo, L. Hu, Rapid liquid phase-assisted ultrahigh-temperature sintering of high-entropy ceramic composites, Sci. Adv. (2022), https://doi.org/10.1126/sciadv.abn8241.

[36] H. Chen, H. Xiang, F.Z. Dai, J. Liu, Y. Zhou, Porous high entropy (Zr0.2Hf0.2Ti0.2Nb0.2Ta0.2)B2: a novel strategy towards making ultrahigh temperature ceramics thermal insulating, J. Mater. Sci. Technol. 35 (2019) 2404–2408, https://doi.org/10.1016/j.jmst.2019.05.059.

[37] H.-R. Mao, E.-T. Dong, S.-B. Jin, X.-M. Qiu, P. Shen, Ultrafast high-temperature synthesis and densification of high-entropy carbides, J. Eur. Ceram. Soc. 42 (2022) 4053–4065, https://doi.org/10.1016/j.jeurceramsoc.2022.03.054.

[38] D. Hedman, A.C. Feltrin, Y. Miyamoto, F. Akhtar, Ab initio aided design of novel quaternary, quinary and senary high-entropy borocarbides, J. Mater. Sci. Submitt. (2021) 422–443, https://doi.org/10.1007/s10853-021-06600-y.

[39] A.C. Feltrin, D. Hedman, F. Akhtar, Transformation of metastable dual-phase (Ti0.25V0.25Zr0.25Hf0.25)B2 to stable high-entropy single-phase boride by thermal annealing, Appl. Phys. Lett. (2021), https://doi.org/10.1063/5.0066698.

[40] M. Biesuz, L. Karacasulu, C. Vakifahmetoglu, V.M. Sglavo, On the temperature measurement during ultrafast high-temperature sintering (UHS): shall we trust metal-shielded thermocouples? J. Eur. Ceram. Soc. (2023) https://doi.org/10.1016/j.jeurceramsoc.2023.11.061.

[41] R. Telle, L.S. Sigl, K. Takagi, Boride-based hard materials (in:), Handb. Ceram. Hard Mater. (2000), https://doi.org/10.1002/9783527618217.ch22.

[42] A.K. Niessen, F.R. De Boer, The enthalpy of formation of solid borides, carbides, nitrides, silicides and phosphides of transition and noble metals, J. Less-Common Met. 82 (1981) 75–80, https://doi.org/10.1016/0022-5088(81)90200-9.

[43] J.M. Lonergan, W.G. Fahrenholtz, G.E. Hilmas, Sintering mechanisms and kinetics for reaction hot-pressed ZrB2, J. Am. Ceram. Soc. (2015), https://doi.org/10.1111/jace.13544.

[44] L. Feng, W.G. Fahrenholtz, G.E. Hilmas, F. Monteverde, Effect of Nb content on the phase composition, densification, microstructure, and mechanical properties of high-entropy boride ceramics, J. Eur. Ceram. Soc. 41 (2021) 92–100, https://doi.org/10.1016/j.jeurceramsoc.2020.08.058.

[45] Y. Zhang, W.M. Guo, Z.Bin Jiang, Q.Q. Zhu, S.K. Sun, Y. You, K. Plucknett, H.T. Lin, Dense high-entropy boride ceramics with ultra-high hardness, Scr. Mater. 164 (2019) 135–139, https://doi.org/10.1016/j.scriptamat.2019.01.021.

[46] J. Gu, J. Zou, S.K. Sun, H. Wang, S.Y. Yu, J. Zhang, W. Wang, Z. Fu, Dense and pure high-entropy metal diboride ceramics sintered from self-synthesized powders via boro/carbothermal reduction approach, Sci. China Mater. (2019), https://doi.org/10.1007/s40843-019-9469-4.

[47] Y. Zhang, Z.Bin Jiang, S.K. Sun, W.M. Guo, Q.S. Chen, J.X. Qiu, K. Plucknett, H. T. Lin, Microstructure and mechanical properties of high-entropy borides derived from boro/carbothermal reduction, J. Eur. Ceram. Soc. 39 (2019) 3920–3924, https://doi.org/10.1016/j.jeurceramsoc.2019.05.017.

[48] Y. Zhang, S.K. Sun, W. Zhang, Y. You, W.M. Guo, Z.W. Chen, J.H. Yuan, H.T. Lin, Improved densification and hardness of high-entropy diboride ceramics from fine powders synthesized via borothermal reduction process, Ceram. Int (2020) 0–1, https://doi.org/10.1016/j.ceramint.2020.02.214.

[49] E. Rudy, S. Windisch, Ternary Phase Equilibria in Transition Metal-Boron-Carbon-Silicon Systems. Part II. Ternary Systems. Vol XIII. Phase Diagrams of the Systems Ti-B-C, Zr-B-C, and Hf-B-C, AFML Technical Report, Part 2, Volume XIII (1966).

[50] S.S. Ordan'yan, A.I. Dmitriev, K.T. Bizhev, E.K. Stepanenko, Interaction in B4C-MeVB2 systems, Sov. Powder Metall. Met. Ceram. 26 (1987) 834–836, https://doi.org/10.1007/BF00794368.

[51] T. Ungár, Microstructural parameters from X-ray diffraction peak broadening, Scr. Mater. 51 (2004) 777–781, https://doi.org/10.1016/j.scriptamat.2004.05.007.

[52] W. Zhang, L. Chen, C. Xu, X. Lv, Y. Wang, J. Ouyang, Y. Zhou, Grain growth kinetics and densification mechanism of (TiZrHfVNbTa)C high-entropy ceramic under pressureless sintering, J. Mater. Sci. Technol. 110 (2022) 57–64, https://doi.org/10.1016/j.jmst.2021.08.070.

[53] M. Qin, J. Gild, C. Hu, H. Wang, M.S.Bin Hoque, J.L. Braun, T.J. Harrington, P. E. Hopkins, K.S. Vecchio, J. Luo, Dual-phase high-entropy ultra-high temperature ceramics, J. Eur. Ceram. Soc. 40 (2020) 5037–5050, https://doi.org/10.1016/j.jeurceramsoc.2020.05.040.

[54] T.J. Harrington, J. Gild, P. Sarker, C. Toher, C.M. Rost, O.F. Dippo, C. McElfresh, K. Kaufmann, E. Marin, L. Borowski, P.E. Hopkins, J. Luo, S. Curtarolo, D. W. Brenner, K.S. Vecchio, Phase stability and mechanical properties of novel high entropy transition metal carbides, Acta Mater. (2019), https://doi.org/10.1016/j.actamat.2018.12.054.

[55] W.G. Fahrenholtz, G.E. Hilmas, I.G. Talmy, J.A. Zaykoski, Refractory diborides of zirconium and hafnium, J. Am. Ceram. Soc. (2007), https://doi.org/10.1111/j.1551-2916.2007.01583.x.

[56] R.G. Munro, Material properties of titanium diboride, J. Res Natl. Inst. Stand Technol. (2000), https://doi.org/10.6028/jres.105.057.

[57] P. Wang, R. Kumar, E.M. Sankaran, X. Qi, X. Zhang, D. Popov, A.L. Cornelius, B. Li, Y. Zhao, L. Wang, Vanadium diboride (VB2) synthesized at high pressure: elastic, mechanical, electronic, and magnetic properties and thermal stability, Inorg. Chem. (2018), https://doi.org/10.1021/acs.inorgchem.7b02550.